Topology of the valley-Chern effect

Kai Qian,[1] David J. Apigo,[1] Camelia Prodan,[1] Yafis Barlas,[2] and Emil Prodan[2,*]
[1]*Department of Physics, New Jersey Institute of Technology, Newark, New Jersey 07102, USA*
[2]*Department of Physics, Yeshiva University, New York, New York 10016, USA*

(Received 22 March 2018; revised manuscript received 18 June 2018; published 24 October 2018)

The quantum valley-Hall effect (QVHE) manifests in both classical and quantum materials as the emergence of pairs of quasichiral bands along certain interfaces. This bulk-boundary principle is well understood in the limit where the valleys result from a slight splitting of Dirac singularities. However, using a versatile experimental platform based on magnetically coupled spinners, we demonstrate that this regime is not suitable for metamaterial applications due to the delocalization of the interface modes. We also find that a strong splitting of the Dirac singularities washes away the QVHE. We then propose that the enlargement of the bulk gap to be accompanied by a Berry curvature engineering that keeps it localized near the valleys. This is a new regime, entirely outside the umbrella of Dirac physics, which we call the valley-Chern effect (VCE). By establishing an exact relation between VCE and quantum spin-Hall effect, we demonstrate a robust bulk-boundary principle, which could be the foundation of a new wave of applications of topological metamaterials.

DOI: 10.1103/PhysRevB.98.155138

I. INTRODUCTION

Graphene and related systems continue to be laboratories for new ideas and sources of remarkable new effects. With its low-energy physics determined by two small pockets of the Brillouin zone graphene led scientists to realize that a new effective observable, the valley, emerges in many physical situations. This observable can be controlled and manipulated like the spin [1–5] when the valley commutes with the dynamics of the low-energy degrees of freedom. If the spectrum is gapped by breaking the inversion symmetry of the honeycomb lattice, a unique topological effect emerges [4,6] (see Ref. [7] for a brief and informative update), the quantum valley-Hall effect (QVHE). It manifests in the emergence of counter-propagating quasichiral modes at the interface between two mirrored samples. QVHE is quite appealing for engineering interface modes because it does not require breaking of the time-reversal symmetry or strong spin-orbit couplings. It has been observed in many solid-state devices [8–12] and the interest continues to be strong, especially in the context of graphene bilayers [13–20]. It has been proposed in many photonic devices [21–26] and it was observed recently in laboratories [27–29]. QVHE has been enthusiastically embraced by the topological mechanics community, where there has been an explosion of laboratory demonstrations of the effect [30–40]. We were particularly motivated by the work of Ruzzene *et al.* [32,33], where the mechanical interface modes have been recorded in real time, providing a dramatic visual demonstration of signal guiding along zigzagged interfaces.

The bulk-boundary principle responsible for the observed interface modes is well understood in the regime where the valleys result from a slight splitting of graphene's Dirac cones [15]. In such cases, the physics of low-energy excitations can be captured by effective Dirac models which only cover the continuum limit, where the domain walls (DW) and the perturbations occur at small energy scales and over length scales much larger than that of the lattice parameters. This regime, unfortunately, is quite far from what is needed for practical applications of metamaterials, where the DWs have to be sharp and the spectral gaps large in order to ensure good localization of the interface modes. These aspects are analyzed in the first part of our work using a novel and versatile experimental platform based on magnetically coupled spinners [41]. Using the standard implementation of the QVHE based on first near-neighbor couplings on a honeycomb lattice, we discover a fundamental conflict, namely, that the effect becomes weaker and weaker as the band gap is increased. This is evidenced through an analysis of the Berry curvature, which washes away as the spectral gap is increased. Experimentally, we demonstrate the existence of the interface modes and study their localization as function of bulk gap, providing irrefutable evidence that practical constraints forces on us, the metamaterials scientists, to exit the regime where Dirac physics applies. In this extra regime, we reproduce the forward propagation along a zigzagged interface, as observed in many studies before us, but we demonstrate, perhaps for the first time, back-scattering of the interface modes under lattice defects. This demonstrates that the effect is only a weak topological effect and brings a cautionary tale about the zigzagged interface test.

Since the protection of the interface modes is not universal, for practical applications, one needs to understand extremely well what are the safe working assumptions. This became a hotly debated issue inside the metamaterials community. The theory based on the Dirac physics supplies the following safe working conditions: the domain walls and the perturbations must occur at small energy scales and over length scales much larger than that of the lattice parameters. This is clearly of very little use for metamaterials applications. Prompted by all

*prodan@yu.edu

the above, we searched and discovered a new regime, which we call the valley-Chern effect, where a robust bulk-boundary principle can be established via topological arguments rather than effective models. This regime is characterized by large bulk spectral gaps and Berry curvature distributions that are entirely concentrated around the valley points. As we already emphasized, this requires Berry curvature engineering achievable only by turning on couplings beyond the first near-neighbors.

We establish an exact connection between the valley-Chern effect (VCE) and the quantum spin-Chern (SC) effect [42,43], with the latter defined here as time-reversal invariant systems with an additional U(1) symmetry. For this, one of our key observations is that a domain-wall configuration can be formally folded into a bilayered configuration with an edge. The valleys of the bulk bilayer now carry integer Chern numbers and a standard topological argument ensures us that the valleys can be trivially continued over the entire Brillouin torus. As such, the valley degrees of freedom become band indices and they can be defined in the real-space representation. As we shall see, this continuation is equivalent to inserting totally disconnected bands, a procedure that does not affect the physics of the original system, and the folded bulk Hamiltonian can be unitarily mapped into a reference SC insulator. By using the well understood bulk-boundary correspondence of the latter as well as the precise relation between the reference SC and VC systems, a generic argument for the existence of the edge modes emerges.

It will become clear that, in the VCE regime, the DW potential can be always optimized in order to generate pairs of chiral DW modes with the following trades of genuine topological bands: (1) they emerge from one bulk band, traverse the bulk gap and dive into the opposite bulk band; (2) they do not back-scatter as long as a certain symmetry is preserved, which steams from the U(1) symmetry of the reference SC insulator. Let us point out that in QVHE, the pseudochiral DW modes reconnect with each other rather than dissolving into the bulk spectrum, which is an inherent source of back-scattering. Furthermore, VCE does not require slow variations of the interface potentials. In fact, our theory predicts the possibility of chiral modes even under potentials which completely decouple the domains, hence in a simple edge configuration. Such chiral modes have been observed recently [37] under specialized boundary conditions.

As the program of Berry curvature engineering is yet to be developed, we will exemplify all these formal arguments on our present experimental model. At this point, we can only provide predictions and recommendations for implementations of true VCE that go beyond the first near-neighbors.

II. COUPLED SPINNERS: A VERSATILE PLATFORM

We describe in this section the experimental platform based on magnetically coupled spinners. The centers of the spinners are pinned, hence they only have a rotational degree of freedom φ. By simply staking two or more spinners on top of each other, we can engineer mechanical building blocks with controlled number of degrees. Furthermore, the centers of the spinners can be pinned in any two-dimensional pattern and the degrees of freedom can be easily coupled in virtually any desirable configuration. The resulting experimental platform is extremely versatile and can be utilized to implement any quadratic two-dimensional discrete Hamiltonian. It will be used in the present work to investigate different QVHE regimes obtained with the classical honeycomb lattice setup.

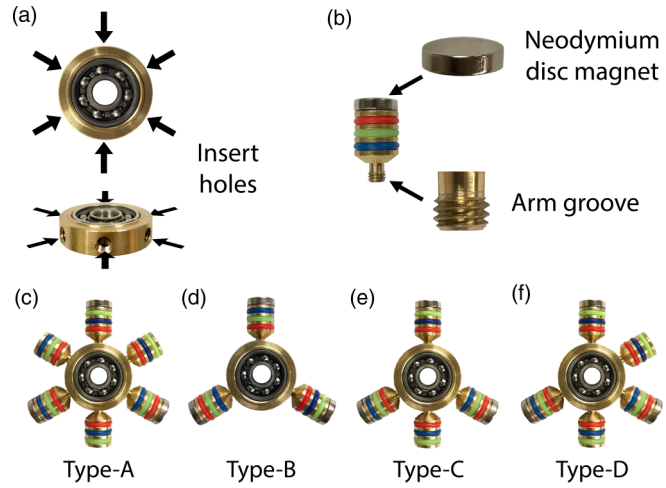

FIG. 1. Configurable spinner with detachable arms. (a) Ball bearing with six inserts. (b) Detachable arms with magnetic ends for coupling. [(c)–(f)] The four spinner configurations used in our study, together with the labels used in the text.

A. Configurable spinners

The configurable spinners are illustrated in Fig. 1. They consist of a stainless steel ball-bearing fixed in a brass encapsulation. The latter is fitted with six grooved indentations as shown in see Fig. 1(a), which enable us to attach additional components. This work features the relatively heavy brass arms shown Fig. 1(b), which can be securely fastened in the brass encapsulation via the end-bolts shown in the inset of Fig. 1(b). The arms are also fitted with strong magnets which provide the coupling between the spinners. Four spinner configurations will be used in our study, displaying six, five, four, and three arms, as shown in Figs. 1(c)–1(f). These configurations will be referred to as A, B, C, and D, respectively.

The uniformity of the arms, their fastening to the encapsulation, the uniformity of the magnets, and the quality of the ball bearings are all essential for the proper functionality of the system. The latter reflects in the high$-Q$ factors of the coupled resonators, which was measured to be around 50.

B. Mapping the basic couplings

In the following, we will concentrate on three basic couplings: A-A, B-B, and A-B. These magnetic couplings can measured by mapping the resonant modes of the corresponding dimers. The dynamics of a dimer is governed by the Lagrangian:

$$L(\varphi_1, \varphi_2, \dot{\varphi}_1, \dot{\varphi}_2) = \tfrac{1}{2} I_1 \dot{\varphi}_1^2 + \tfrac{1}{2} I_2 \dot{\varphi}_2^2 - V(\varphi_1, \varphi_2). \quad (1)$$

In the regime of small oscillations around the equilibrium configuration $\varphi_1 = \varphi_2 = 0$, the potential can be replaced by

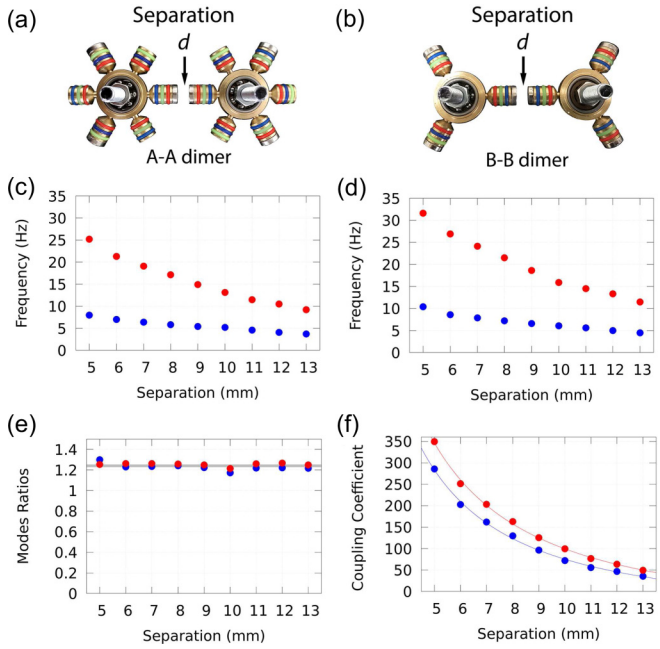

FIG. 2. Mapping the coupling coefficients. [(a) and (b)] The A-A and B-B dimmer configurations, respectively. (c) The experimentally measured resonant frequencies $f_{\pm}^{A-A}$ (red/blue dots, respectively) of the A-A dimer as functions of separation d between the magnets. (d) Same as (c) but for B-B dimer. (e) The ratios f_{+}^{B-B}/f_{+}^{A-A} (red dots) and f_{-}^{B-B}/f_{-}^{A-A} (blue dots) as a function of separation. (f) The coupling coefficients α (solid red dots) and β (solid blue dots), as derived from (6) in units of $4\pi^2 I_A \times \mathrm{Hz}^2$, together with the analytic fits (7) (continuous lines).

its quadratic approximation:

$$V(\varphi_1,\varphi_2) = V_0 + \tfrac{1}{2}\alpha\left(\varphi_1^2+\varphi_2^2\right) + \beta\varphi_1\varphi_2. \tag{2}$$

The symmetry of the potential with respect to the exchange $1 \leftrightarrow 2$ is made explicit in this expansion. We will refer to α and β as the coupling coefficients and, from stability considerations, $|\beta| < \alpha$. Also, β happens to be positive in our setup, but one should keep in mind that negative β's can be also engineered, if needed. The equations of motion are straightforward:

$$I_j\ddot{\varphi}_j + \alpha\varphi_j + \beta\varphi_{j'} = 0, \quad j = 1,2, \quad j' = 2,1. \tag{3}$$

With the ansatz $\varphi_j(t) = \frac{1}{\sqrt{I_j}}A_j e^{i\omega t}$, $\omega = 2\pi f$, the equation for the resonant modes reads

$$\omega^2\begin{pmatrix}A_1\\A_2\end{pmatrix} = \begin{pmatrix}\frac{\alpha}{I_1} & \frac{\beta}{\sqrt{I_1 I_2}}\\ \frac{\beta}{\sqrt{I_1 I_2}} & \frac{\alpha}{I_2}\end{pmatrix}\begin{pmatrix}A_1\\A_2\end{pmatrix}. \tag{4}$$

For $I_1 = I_2 = I_A$ or I_B, it leads to the pairs of resonant frequencies

$$f_{\pm}^{A-A} = \sqrt{\frac{\alpha\pm\beta}{4\pi^2 I_A}}, \quad f_{\pm}^{B-B} = \sqrt{\frac{\alpha\pm\beta}{4\pi^2 I_B}}. \tag{5}$$

The upper/lower frequency modes correspond to motions where the two angles are locked as $\varphi_2 = \pm\varphi_1$, respectively.

The resonant frequencies have been independently measured as functions of distance d between the magnets and

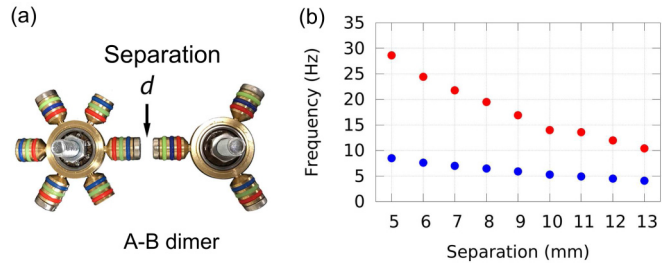

FIG. 3. The A-B coupling. (a) The A-B dimer configuration. (b) The experimentally measured resonant frequencies $f_{\pm}^{A-B}$ as a function of distance between the magnets.

the data is reported in Figs. 2(c) and 2(d). We have verified that the coupling coefficients are not affect by the removal of the arms, by examining the ratios $f_{\pm}^{B-B}/f_{\pm}^{A-A}$. As one can see in Fig. 2(e), these two ratios are more or less identical and independent of d. From (5), this constant value can be identified with the ratio $\sqrt{\frac{I_A}{I_B}}$, which comes to 1.235 from a fit. At this point, we obtained a quantitative measure of $r = I_A/I_B = 1.525$. Furthermore, it is possible to invert any of the relations in (5), e.g., A-A, and map the coupling coefficients

$$\alpha = 2\pi^2 I_A(f_+^2 + f_-^2), \quad \beta = 2\pi^2 I_A(f_+^2 - f_-^2). \tag{6}$$

The resulting values are shown in Fig. 2(f), in convenient units of $4\pi^2 I_A \times \mathrm{Hz}^2$, together with the theoretical fits

$$\alpha(d) = -\frac{654.09}{\sqrt{d}} + \frac{2763.66}{d} + \frac{575.89}{d^2},$$
$$\beta(d) = -\frac{778.14}{\sqrt{d}} + \frac{3439.81}{d} + \frac{161.35}{d^2}. \tag{7}$$

For completeness, the resonant frequencies for the A-B dimer are reported in Fig. 3. They agree well with the coupling coefficients (7). Similar measurements have been performed for the combinations A-C and A-D, for which the coupling coefficients remain the same and r was found to be approximately 1.3 and 1.2, respectively.

III. QUANTUM VALLEY-HALL EFFECT WITH COUPLED SPINNERS

We will generate the QVHE with the classical honeycomb configuration. The fully assembled spinner system in the A-B configuration is shown in Fig. 4, together with the primitive cell and primitive vectors. The latter have been chosen purposely that way to conform with the domain wall introduced later. The centers of the primitive cells are located at $\boldsymbol{R_n} = n_1\boldsymbol{a}_1 + n_2\boldsymbol{a}_2$, hence we can label the cells by $\boldsymbol{n} = (n_1, n_2) \in \mathbb{Z}^2$. The spinners can be easily identified using the pair of indexes $(\boldsymbol{n}, A)$ or $(\boldsymbol{n}, B)$. The shift operations acting on the indices

$$S_1\boldsymbol{n} = S_1(n_1,n_2) = (n_1+1, n_2),$$
$$S_2\boldsymbol{n} = S_2(n_1,n_2) = (n_1, n_2+1), \tag{8}$$

will prove to be convenient for the calculations below.

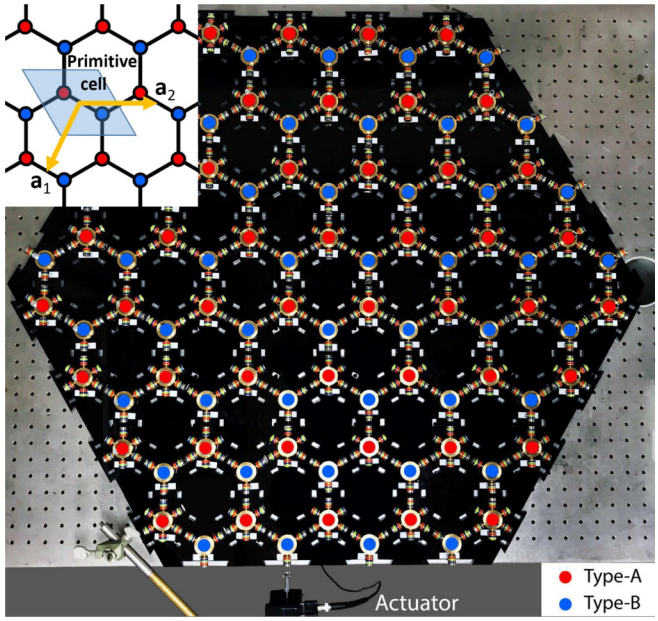

FIG. 4. Bulk configuration. It is a finite bipartite honeycomb lattice populated with A (red) and B (blue) type spinners. The actuator appears at the bottom of the illustration. For technical specifications, see Sec. III E. The inset shows the primitive cell (shaded area) and the primitive vectors $\boldsymbol{a}_{1,2}$.

A. Mapping the bulk spectrum

The Lagrangian of the infinite lattice takes the form

$$\mathcal{L} = \sum_{\boldsymbol{n}\in\mathbb{Z}^2} \left(\frac{1}{2} I_A \dot{\varphi}^2_{\boldsymbol{n},A} + \frac{1}{2} I_B \dot{\varphi}^2_{\boldsymbol{n},B} - V(\varphi_{\boldsymbol{n},A}, \varphi_{\boldsymbol{n},B}) \right) - V\left(\varphi_{\boldsymbol{n},A}, \varphi_{S_1^{-1}S_2^{-1}\boldsymbol{n},B}\right) - V\left(\varphi_{\boldsymbol{n},A}, \varphi_{S_2^{-1}\boldsymbol{n},B}\right), \tag{9}$$

and, using the quadratic approximation (2), the equations of motions take the form

$$\begin{pmatrix} I_A \ddot{\varphi}_{\boldsymbol{n},A} \\ I_B \ddot{\varphi}_{\boldsymbol{n},B} \end{pmatrix} = \begin{pmatrix} -3\alpha\varphi_{\boldsymbol{n},A} - \beta\left(\varphi_{\boldsymbol{n},B} + \varphi_{S_1^{-1}S_2^{-1}\boldsymbol{n},B} + \varphi_{S_2^{-1}\boldsymbol{n},B}\right) \\ -3\alpha\varphi_{\boldsymbol{n},B} - \beta\left(\varphi_{\boldsymbol{n},A} + \varphi_{S_1S_2\boldsymbol{n},A} + \varphi_{S_2\boldsymbol{n},A}\right) \end{pmatrix}. \tag{10}$$

It is convenient to make the change of variables

$$\varphi_{\boldsymbol{n},A} = \frac{1}{\sqrt{I_A}} \psi_{\boldsymbol{n},A}, \quad \varphi_{\boldsymbol{n},B} = \frac{1}{\sqrt{I_B}} \psi_{\boldsymbol{n},B}, \tag{11}$$

and bring the equations to the form

$$\begin{pmatrix} \ddot{\psi}_{\boldsymbol{n},A} \\ \ddot{\psi}_{\boldsymbol{n},B} \end{pmatrix} = \begin{pmatrix} -3\frac{\alpha}{I_A}\psi_{\boldsymbol{n},A} - \frac{\beta}{\sqrt{I_A I_B}}\left(\psi_{\boldsymbol{n},B} + \psi_{S_1^{-1}S_2^{-1}\boldsymbol{n},B} + \psi_{S_2^{-1}\boldsymbol{n},B}\right) \\ -3\frac{\alpha}{I_B}\psi_{\boldsymbol{n},B} - \frac{\beta}{\sqrt{I_A I_B}}\left(\psi_{\boldsymbol{n},A} + \psi_{S_1S_2\boldsymbol{n},A} + \psi_{S_2\boldsymbol{n},A}\right) \end{pmatrix}. \tag{12}$$

We can encode the degrees of freedom in a single function:

$$\boldsymbol{\psi} : \mathbb{Z}^2 \to \mathbb{C}^2, \quad \boldsymbol{\psi}(\boldsymbol{n}) = \begin{pmatrix} \psi_{\boldsymbol{n},A} \\ \psi_{\boldsymbol{n},B} \end{pmatrix}, \tag{13}$$

and use the ansatz $\boldsymbol{\psi}(t) \to \mathrm{Re}[e^{i\omega t}\boldsymbol{\psi}]$, $\omega = 2\pi f$. Then, in the units used in Fig. 2, the equations of motions simplify to

$$f^2\boldsymbol{\psi} = \left[\tfrac{3}{2}\alpha(1 + r + (1-r)\sigma_3) + \beta\sqrt{r}(\sigma_1 + \sigma_-(S_1S_2 + S_2) + \sigma_+(S_1^\dagger S_2^\dagger + S_2^\dagger))\right]\boldsymbol{\psi}, \tag{14}$$

where the shift operators act as

$$(S_j\boldsymbol{\psi})(\boldsymbol{n}) = \boldsymbol{\psi}(S_j\boldsymbol{n}), \quad j = 1, 2, \tag{15}$$

and σ's are Pauli's matrices. The shift operators commute with each other and also with the dynamical matrix and have common eigenvectors:

$$S_j\, e^{i\boldsymbol{k}\boldsymbol{n}} = e^{ik_j} e^{i\boldsymbol{k}\cdot\boldsymbol{n}}, \quad \boldsymbol{k} = (k_1, k_2) \in [-\pi, \pi]^2, \quad j = 1, 2. \tag{16}$$

Hence the normal modes will be sought in the form $\boldsymbol{\psi}(\boldsymbol{n}) = e^{i\boldsymbol{k}\cdot\boldsymbol{n}}\,\xi$, $\xi \in \mathbb{C}^2$, in which case the dispersion equation reduces further to

$$f^2\xi = \left[\frac{3}{2}\alpha(1 + r + (1-r)\sigma_3) + \beta\sqrt{r}\begin{pmatrix} 0 & \gamma(\boldsymbol{k})^* \\ \gamma(\boldsymbol{k}) & 0 \end{pmatrix}\right]\xi, \tag{17}$$

with $\gamma(\boldsymbol{k}) = 1 + e^{i(k_1+k_2)} + e^{ik_2}$. The explicit dispersion equations of the resonant modes then follow:

$$f_\pm = \frac{3\alpha}{2}\left[(1+r) \pm \sqrt{(1-r)^2 + \frac{4r\beta^2}{9\alpha^2}|\gamma(\boldsymbol{k})|^2}\right]^{\frac{1}{2}}. \tag{18}$$

When $r = 1$, the system is inversion symmetric and two Dirac singularities are present in the bulk band structure. The imbalance between I_A and I_B breaks the inversion symmetry, hence the Dirac singularities split as soon as $r > 1$. Let us note that the valleys are located at the points where $|\gamma(\boldsymbol{k})| = 0$, which are $K = -K' = (\frac{2\pi}{3}, -\frac{2\pi}{3})$.

A graphical representation of the dispersion equations (18) is reported in Fig. 5 for a sequence of increasing values of r. For the value $r = 1.525$ corresponding to the A-B configuration, a comparison between the theoretical spectrum and the experimental reading from a sensor placed inside the structure is shown in Fig. 6. Since the structure is actuated from the edge, a nonzero reading from the sensor indicates that

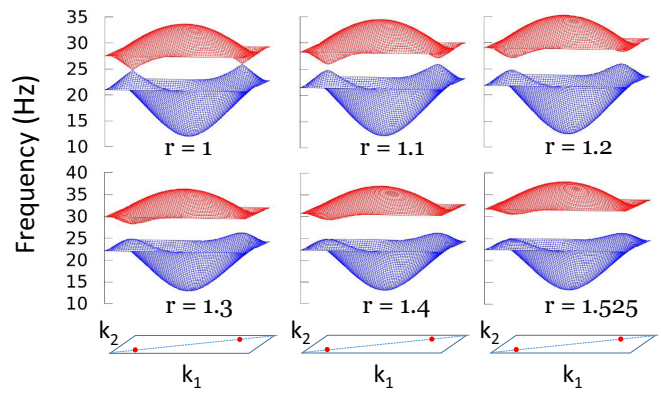

FIG. 5. Predicted bulk band spectra. Plots of the dispersion equations (18) for various values of the ratio $r = I_A/I_B$. The graphs are rendered as functions of $(k_1, k2) \in [-\pi, \pi]^2$ and the red dots indicate the position of the valleys points K and K'.

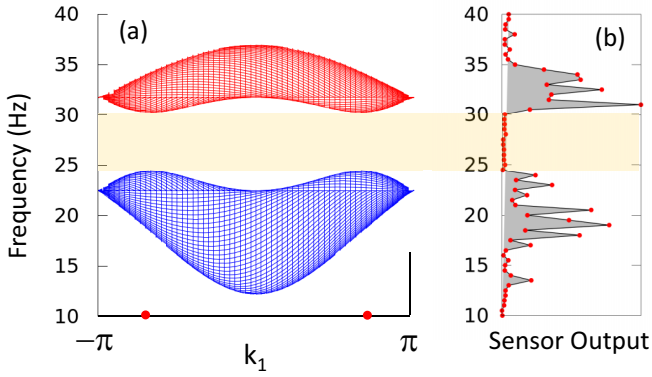

FIG. 6. Predicted vs measured bulk spectrum. (a) The theoretical data taken from the last panel of Fig. 5 ($r = 1.525$). The view point is chosen here such that k_2 is into the page and the red dots indicate the position of the valleys K and K'; (b) The reading from a sensor placed inside the spinner structure when the system is actuated from the edge, as seen in Fig. 4. The shaded area marks the spectral gap.

the actuating frequency belongs to the bulk spectrum, while a zero reading indicates that it is in a spectral gap. Using this criterion, we found that the predicted spectral gap in Fig. 6 is confirmed by the experiment within 1%. The details of the measurements are reported in Sec. III E.

There are several important observations about the bulk dynamics. First, let us recall that one pre-requisite for QVHE is a well defined pair of valleys. Looking at the expressions (18), one sees that the depth of the valleys is set by the ratio β/α, once r is fixed. The larger this ratio the deeper the valleys, but note that $\beta/\alpha < 1$, so with a first nearest neighbor coupling design on the honeycomb lattice, there is an upper limit on the sharpness of the valleys. Note that for our experimental system $\beta/\alpha = 0.8$, placing it among the most optimized systems ever produced. As such, the conclusions we draw based on our experimental setup have quite a broad relevance.

Secondly, let us point out that, while the dynamical matrix in (17) can be indeed approximated by a Dirac Hamiltonian around the valleys K and K', by a simple linear expansion, the region on which this approximation holds reduces drastically with the increase of r. This can be already seen by examining the spectra in Fig. 5, from where we concluded that treating QVHE with the effective Dirac approximation is questionable at and beyond $r = 1.2$.

B. Berry curvature analysis

For a two-band model, the gap projector can always be expressed as

$$P_G(\boldsymbol{k}) = \tfrac{1}{2}(I - \boldsymbol{n}(\boldsymbol{k})\cdot\boldsymbol{\sigma}), \quad |\boldsymbol{n}(\boldsymbol{k})| = 1, \tag{19}$$

in which case the Berry curvature reduces to

$$F(\boldsymbol{k}) = \pi\, \boldsymbol{n}\cdot\left(\partial_{k_1}\boldsymbol{n}\times\partial_{k_2}\boldsymbol{n}\right). \tag{20}$$

In our case,

$$\boldsymbol{n}(\boldsymbol{k}) = \frac{(g\mathrm{Re}[\gamma(\boldsymbol{k})], g\mathrm{Im}[\gamma(\boldsymbol{k})], -1)}{\sqrt{1+g^2|\gamma(\boldsymbol{k})|^2}}, \quad g = \frac{2\sqrt{r}\beta}{3\alpha(r-1)}, \tag{21}$$

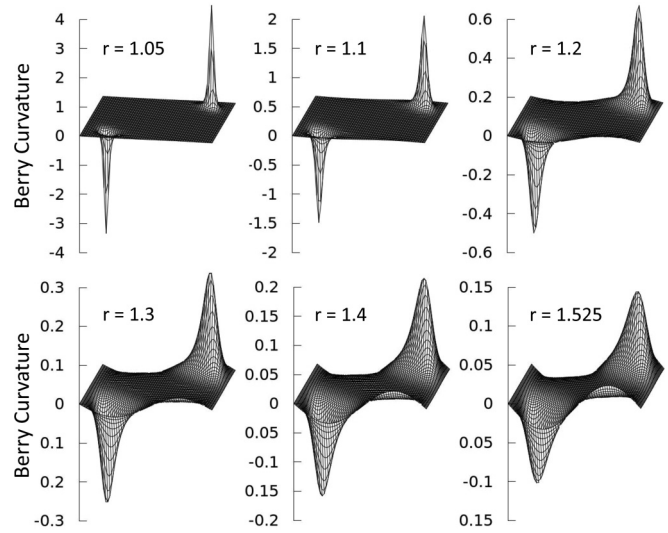

FIG. 7. Berry curvature. The theoretical calculations were performed with the experimental values of the coupling constants α and β and for the specified values of $r = I_A/I_B$. The last value $r = 1.525$ is used in the experimental demonstrations. The data is rendered as function of $(k_1, k2)$ whose axes are not shown.

which leads to the simple expression

$$F(\boldsymbol{k}) = \frac{1}{4\pi}\frac{g^2\sin(k_1)}{(1+g^2|\gamma(\boldsymbol{k})|^2)^{3/2}}. \tag{22}$$

A graphical representation is reported in Fig. 7 for various values of the parameter $r = I_A/I_B$.

There are several important remarks here. First, as expected, if the inversion symmetry is only slightly broken, such as when $r = 1.05$, we see that the Berry curvature is strongly localized near the valleys. But as r is increased, this localization becomes worse, as it can be easily assessed in Fig. 7. A quantitative measure of this localization is the integral of the Berry curvature over half of the Brillouin torus, $-\pi \leqslant k_1 \leqslant 0$, which gives 0.444, 0.395, 0.355, 0.320, and 0.284 for $r = 1.1$, 1.2, 1.3, 1.4, and 1.525, respectively. This somewhat surprising rapid decrease is due to, in part, the slow decay at infinity of the Berry curvature supported by a split Dirac cone.

Those numbers confirm again that one has to be cautious when using Dirac effective models for and beyond $r = 1.2$. Furthermore, it becomes quite apparent that robust QVHE, primed for applications, cannot be generated via simple Dirac cone splittings and instead it will require sophisticated Berry curvature engineering. Let us remind that our experimental model is highly optimized, hence the above warning signs apply to any model based on first nearest neighbor coupling on honeycomb lattice.

C. Domain-wall analysis

The experimental setup with a straight DW is shown in Fig. 8. A schematic of it together with some geometrical data are supplied in Fig. 9. It is important to note that the previously chosen primitive cell and vectors are consistent with the DW,

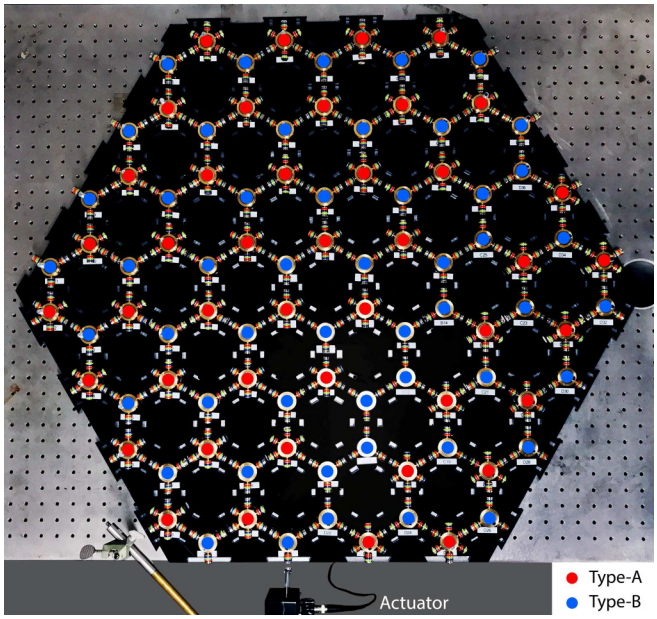

FIG. 8. The experimental setup with a straight domain wall. The domain wall consists of the zigzag chain of B type (blue) spinners. Note the actuator positioned at one end of the domain wall.

in the sense that the domain does not slices the unit cell and the primitive vector $\boldsymbol{a}_1$ is parallel to the DW.

We place the DW between $n_2 = -1$ and $n_2 = 0$ such as the reflection $\mathcal{I}$ ($\mathcal{I}^* = \mathcal{I}$, $\mathcal{I}^2 = I$), acting as $\mathcal{I}|n_1, n_2, A\rangle = |n_1, -n_2 - 1, B\rangle$ and $\mathcal{I}|n_1, n_2, B\rangle = |n_1, -n_2 - 1, A\rangle$, maps the left and right sides of the DW into each other. To determine the dispersion equation, note that, as we cross the interface, the coupling coefficients α and β remain the same and the only effect is the exchange of I_A and I_B. Hence, in the presence of the DW:

$$\omega^2(I - \delta I\, \sigma_3\, \mathrm{sgn}(X_2))\boldsymbol{\varphi} = D\boldsymbol{\varphi}, \tag{23}$$

where $I = \frac{1}{2}(I_A + I_B)$ and $\delta I = \frac{1}{2}(I_A - I_B)$, as well as

$$\mathrm{sgn}(X_2) = \sum_{n,m} \mathrm{sgn}(n)\, |m, n\rangle\langle m, n|, \tag{24}$$

with the convention that $\mathrm{sgn}(0) = 1$.

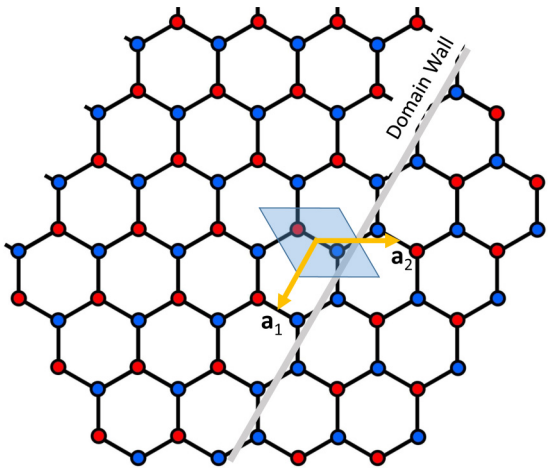

FIG. 9. Schematic of the domain wall. Note that the domain wall does not cut any of the primitive cells.

The left hand side of Eq. (23) is a compact way of saying that the moments of inertia have different values on the two domains. The dynamical matrix in (23) is same as in (10):

$$D = 3\alpha + \beta(\sigma_1 + \sigma_-(S_1 S_2 + S_2) + \sigma_+(S_2^\dagger S_1^\dagger + S_2^\dagger)). \tag{25}$$

We transform (23) in a standard eigen-system problem by performing the transformation

$$\boldsymbol{\varphi} = (I - \delta I\, \sigma_3\, \mathrm{sgn}(X_2))^{-\frac{1}{2}}\boldsymbol{\psi}, \tag{26}$$

in which case the dispersion equation becomes

$$\omega^2\boldsymbol{\psi} = (I - \delta I\, \sigma_3\, \mathrm{sgn}(X_2))^{-\frac{1}{2}}\, D\, (I - \delta I\, \sigma_3\, \mathrm{sgn}(X_2))^{-\frac{1}{2}}\boldsymbol{\psi}. \tag{27}$$

Note that, with $\Gamma = \frac{1}{2}(\frac{1}{\sqrt{I_A}} + \frac{1}{\sqrt{I_B}})$ and $\Delta = \frac{1}{2}(\frac{1}{\sqrt{I_A}} - \frac{1}{\sqrt{I_B}})$,

$$(I - \delta I\, \sigma_3\, \mathrm{sgn}(X_2))^{-\frac{1}{2}} = \Gamma - \Delta\, \sigma_3\, \mathrm{sgn}(X_2). \tag{28}$$

Lastly, because S_1 commutes with the dynamical matrix in (27), we can seek the modes in the form

$$\boldsymbol{\psi}(n_1, n_2) = \mathrm{Re}[e^{ikn_1}\boldsymbol{\xi}_k(n_2)], \quad k \in [-\pi, \pi], \tag{29}$$

in which case the dispersion equation takes the form $H(k)\boldsymbol{\xi}_k = \omega_k^2\boldsymbol{\xi}_k$, where H takes the explicit expression

$$H(k) = (\Gamma - \Delta\sigma_3 \mathrm{sgn}(X_2))\, D_k\, (\Gamma - \Delta\sigma_3 \mathrm{sgn}(X_2)), \tag{30}$$

with D_k derived directly from (25),

$$D_k = 3\alpha + \beta(\sigma_1 + (e^{ik} + 1)\sigma_- S_2 + (e^{-ik} + 1)\sigma_+ S_2^\dagger). \tag{31}$$

The action of $H(k)$ on the basis of $\mathbb{C}^2 \otimes \ell^2(\mathbb{Z})$,

$$|n, +1\rangle = \begin{pmatrix} |n\rangle \\ 0 \end{pmatrix}, \quad |n, -1\rangle = \begin{pmatrix} 0 \\ |n\rangle \end{pmatrix}, \tag{32}$$

can be written explicitly ($s = \pm 1$) as

$$\begin{aligned} H(k)\,|n, s\rangle &= 3\alpha(\Gamma - s\Delta\, \mathrm{sign}(n))^2|n, s\rangle \\ &+ \beta(\Gamma^2 - \Delta^2)|n, -s\rangle + \beta(\Gamma^2 - \Delta^2)(e^{isk} + 1) \\ &\times |n + s, -s\rangle. \end{aligned} \tag{33}$$

The resulting spectrum for the domain-wall configuration of Fig. 8 is reported in Fig. 10, which reproduces the well-known QVHE features. First thing to notice is that the DW modes do not dive into the bulk spectrum but rather get connected at higher and lower energies. This is one difference between this effect and a true topological effect. Also, as r is increased, the bulk gap increases, hence strengthening the localization of the interface modes along DW, but, unfortunately, the DW bands move away from the bulk spectrum and the system will eventually become gapped.

D. Experimental observation of the DW modes

The DW has been actuated from one end, as shown in Fig. 8, until a stationary regime was established. In this setup, the counter-propagating DW modes are scattered into each other at the ends of the interface, leading to a standing wave. Pick-up coils similar to the ones found in electric guitars have been placed on top of the bonds and the standing wave pattern was mapped out. While the details of the measurements are provided in the following section, let us mentioned that four

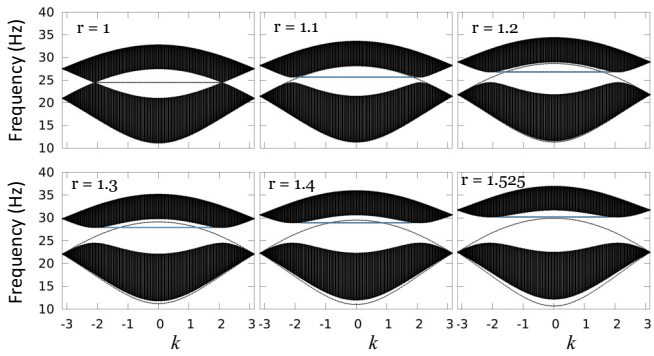

FIG. 10. Predicted spectrum in the presence of a domain wall. Simulations are shown for increasing values of $r = \frac{I_A}{I_B}$, ranging from 1 all the way to the experimental value of 1.525. The spectrum is computed on a strip with the domain-wall at the center. The doubly degenerated flat band seen in all panels is located at the edges of the ribbon, hence it is unrelated to the physics studied here. They have been colored in blue for reader's convenience.

magnetic bonds in the $\boldsymbol{a}_2$ direction have been probed, starting from the DW, enough to asses the spatial localization of the modes.

The results obtained with A/B spinners (hence $r = 1.525$) are reported in Fig. 11. One can see there that, for frequencies up to 25 Hz, the sensors return only small motion amplitudes. These frequencies must be within or very close to the bulk spectrum in which case the signal from the actuator disperses throughout the entire lattice, hence explaining the small amplitudes. Beyond 25 Hz, the sensors pick-up strong amplitudes near the interface and the amplitudes are seen to fade away into the bulk. We are definitely witnessing a standing wave supported by the interface channels. The strongest resonant patterns are observed within 28–29 Hz range of frequencies. Above this range, the sensor readings are seen again to fade away signaling that the frequency approaches the upper part of the bulk spectrum.

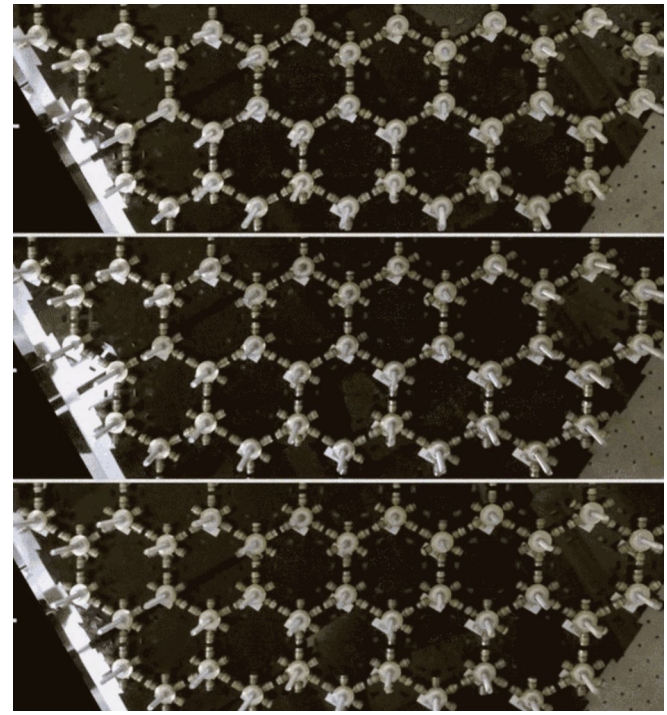

FIG. 12. DW modes along straight interfaces. The panels show the interfaces obtained with the A-B ($r = 1.525$, top), A-C ($r = 1.3$, middle), and A-D ($r = 1.2$, bottom) configurations of the spinner system. The DW modes are actuated from the left (see white arrow). Video recordings of the DW modes are reported in Ref. [44].

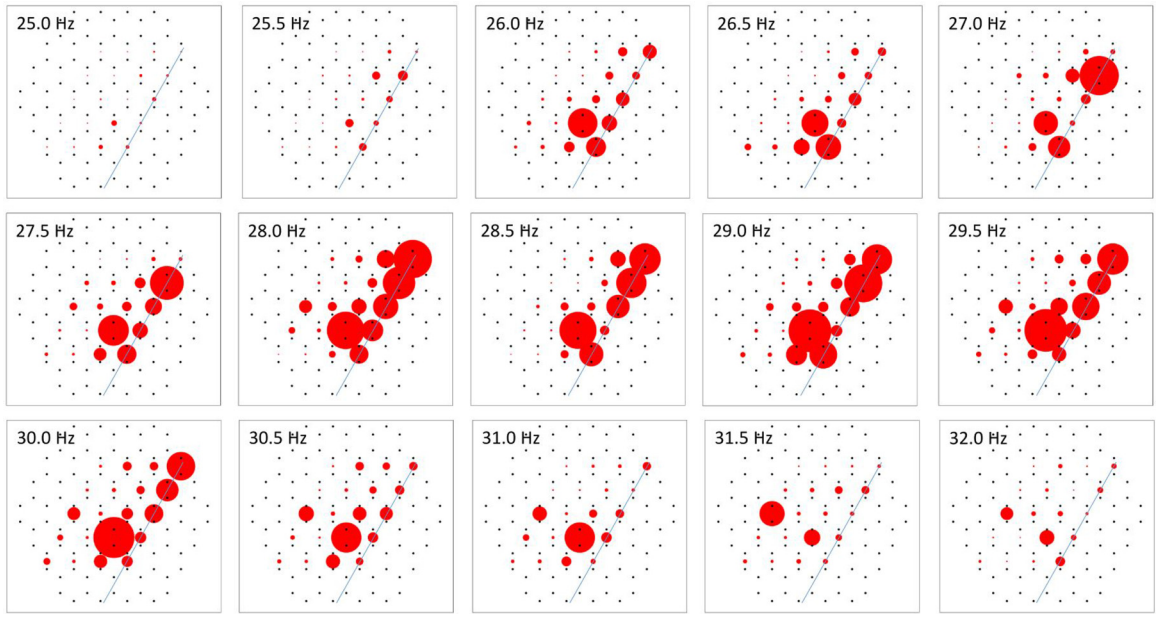

FIG. 11. Experimental observation of the DW modes. The fine line marks the position of the interface relative to the honeycomb lattice, indicated by the black dots. The red disks mark the position of the motion sensors, which are placed above bonds. The size of a disk is proportional with the reading of the motion sensor at that location. The frequencies, which are marked in each panel, sample the entire bulk gap. The measurement are for the A-B system ($r = 1.525$).

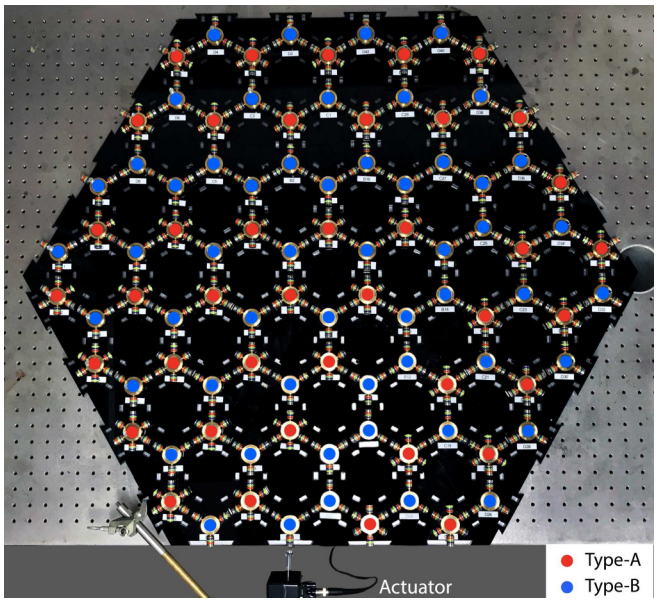

FIG. 13. The experimental setup with an L-shape domain wall. The domain wall consists of the zig-zag chain of B-type (blue) spinners. Note again the actuator positioned at one end of the domain wall.

In Fig. 12 and Ref. [44], we report a comparison between the DW modes generated with A-B ($r = 1.52$), A-C ($r = 1.3$), and A-D ($r = 1.2$) systems. Given that the actuation was identical, the difference between the modes is striking. Indeed, for $r = 1.525$ case, the mode is highly localized and the amplitude of the oscillations is substantial, while for the $r = 1.3$ and $r = 1.2$ cases, the mode is quite delocalized and, because of that, the amplitudes of the oscillations are much smaller. In fact, with $r = 1.2$, it was difficult to observe the DW mode. The inherent conclusion is that the regime $r < 1.2$, where the effective Dirac models apply, is interesting for demonstration purposes but has little relevance for the practical applications.

The DW modes in QVHE are known to be robust against spatially slow deformations of the interface. However, it has been reported in many occasions [30–35,37–40] that a signal can propagate along the domain-wall channels with very little back-reflection, even if the interface is bent sharply. To investigate this interesting and potentially important effect, we reconfigured our A-B system in the L-shaped DW configuration shown in Fig. 13. The measurements have been repeated and the results are reported in Fig. 14. As many before us, we find that, indeed, there is a healthy transmission of the signal beyond the corner of the L-shaped DW. However, judging by the amplitudes seen along the two arms of the L shape (see especially the panels $f = 28.5$ Hz and $f = 29$ Hz), we concluded that the transmission is only about 90%.

Figure 15 and Ref. [45] report video recordings of the L-shaped DW mode, actuated in various conditions. The first panel of Fig. 15 shows a clean interface and the corresponding video recording of the DW mode, supplied in Ref. [45], confirms the conclusion drawn above and the data in Fig. 14. We want, however, to clarify that lack of back scattering in zigzagged interfaces might not have much to do with topological protection. In our case, the wave carries only angular and no linear momentum, so corners have little effect on the wave propagation. This is also the case for the transversal mechanical waves in plates, but corner-passing has been observed with acoustic waves [31], which are longitudinal. The latter observation was in the regime of highly delocalized DW modes, though, and also, note that back-scattering require a high air-pressure point at the corner, which cannot develop in the zigzag geometry. To investigate this issue further, we show in the last two panels of Fig. 15 interfaces where one spinner has been removed from the lower/upper arms of the L shape. As one can see in the video recordings of the DW modes [45], while the domain-wall modes appear to defy sharp corners,

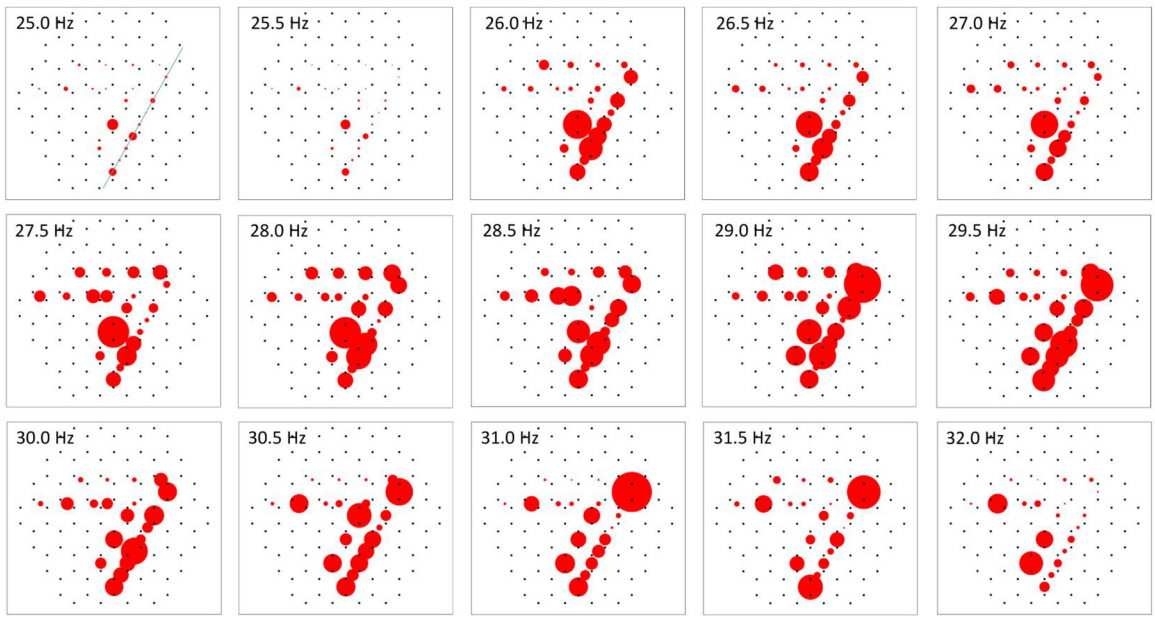

FIG. 14. Experimental observation of the L-shaped domain-wall modes. Except for the shape of the interface, the rest of the details are as in Fig. 11.

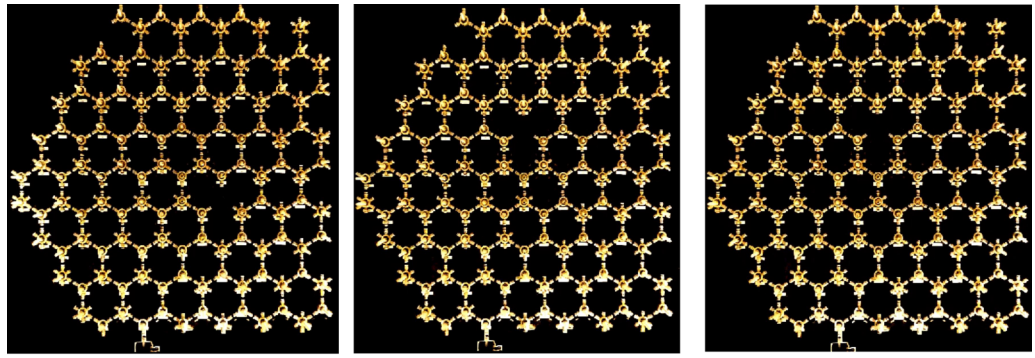

FIG. 15. DW modes along L-shaped interfaces. The panels show L-shaped interfaces obtained with the A-B ($r = 1.525$) spinner configurations. The interface in the left panel is defect-free while in the middle and right panels a defect has been placed on the lower and upper arms of the L shape, respectively. DW modes are actuated from the bottom. Video recordings of the DW modes are reported in Ref. [45].

they are fully back-reflected when a spinner at the interface is jammed or removed. This behavior is in stark contrast with the edge excitations reported in Ref. [46], where the modes of the mechanical Chern insulator are seen to find new propagation paths when obstructions are imposed. This clearly demonstrates that QVHE is only a weak topological effect.

E. Experimental details and media files

One issue we faced right from the beginning is the large size of a fully self-assembled system. An effective solution we found was to divide the base that supports the assemblage in smaller panels which interlock one in another like a jigsaw puzzle. Henceforth, we laser cut 6-mm-thick acrylic panels and fitted them with holes such that, when assembled, the holes generate a honeycomb lattice. The ball bearings shown in Fig. 1(a) were secured in place using zinc carriage bolts and the distance from spinners to base was maintained uniformly throughout the system with washers and nuts. Such panels can be readily assembled and then taken apart for storage or transportation. For example, this practical feature enabled us to demonstrate the topological boundary modes in front of several audiences.

The particular configurations shown in Figs. 8 and 13 were realized with eight acrylic panels and ninety six spinners. The ball bearings were fitted with arms and coupled by neodymium disk magnets, which were secured at the ends of specific arms with super glue. The distance between adjacent magnets (always of opposite polarity) was 7.0 mm. Different configurations of the spinners can be achieved as illustrated in Fig. 1. Prior to running an experiment, all ball bearings were lubricated with silicone oil and the spinner arms were checked for tightness. We found that the connection arms need to be actually glued into place (we used Loctite Threadlocker Red 271 glue).

The lattice was actuated by a Pasco WA-9857 string vibrator, whose arm was fitted with a neodymium disk magnet and placed next to a connecting spinner arm, with the distance between the two held at 7.0 mm. The actuator was computer controlled by a custom LabVIEW software that drives a Rigol DG1022 function generator. That signal was amplified by a Crown XLS 2502 power amplifier with gain set to 5. Frequency sweeps between 8.0 and 40.0 Hz with two different frequency step sizes (0.5 and 0.1 Hz) were performed.

The data were collected by commercially available induction coil sensors, which were placed perpendicular and symmetrically on top of the magnetic bonds between spinners. Special place-holders were 3d-printed and hole locations were laser-cut into the base to ensure that the sensors are always placed in the same geometry relative to the arms. These sensors generate a time-oscillatory output, proportional to the rate of variation of the magnetic flux through the pick-up coil. In turn, these rates are proportional to the speed of the arms. For each frequency, the outputs were recorded and their root mean squares were extracted. The latter are proportional with the amplitudes of oscillations of the spinners and were used to generate the plots in Figs. 11 and 14.

IV. BEYOND QVHE: THE TOPOLOGICAL VALLEY-CHERN EFFECT

QVHE is associated with and explained by Dirac effective models. As revealed by our experimental investigations, the regime where these effective models apply is not optimal for practical applications. In this section, we identify, define and characterize the valley-Chern effect, which can occur in regimes where the Dirac effective models can fail completely.

A. The Regime of valley-Chern effect

The reader can find here the precise conditions where VCE can be observed. The degrees of freedom per primitive cell will be fixed at two but at no point our theory is conditioned by that choice. The choice was mainly made to keep our diagrams simple.

Henceforth, let

$$H : \mathbb{C}^2 \otimes \ell^2(\mathbb{Z}^2) \to \mathbb{C}^2 \otimes \ell^2(\mathbb{Z}^2) \tag{34}$$

be a bulk Hamiltonian

$$H = \sum_{\boldsymbol{x},\boldsymbol{x}' \in \mathbb{Z}^2} h_{\boldsymbol{x}-\boldsymbol{x}'} \otimes |\boldsymbol{x}\rangle\langle \boldsymbol{x}'|, \quad h^{\dagger}_{\boldsymbol{x}-\boldsymbol{x}'} = h_{\boldsymbol{x}'-\boldsymbol{x}} \tag{35}$$

over a lattice with two degrees of freedom per primitive cell. Above, $\mathbb{Z}^2$ is not to be confused with a square lattice as it only

serves as labels for the primitive cells. The primitive cell and the labels are assumed to be consistent with a domain wall (DW), to be imposed later. More precisely, the shift operators $S_\parallel|n,m\rangle = |n+1,m\rangle$ and $S_\perp|n,m\rangle = |n,m+1\rangle$ act parallel and across the DW. The Hamiltonian can be expressed in terms of these shift operators and, by using their common eigenmodes, $\varphi_{\boldsymbol{k}} = \sum_{n,m\in\mathbb{Z}} e^{\imath(k_\parallel n + k_\perp m)}|n,m\rangle$, one can easily move between the real and quasimomentum representations [$\boldsymbol{k} = (k_\parallel, k_\perp)$]:

$$H = \sum_{\boldsymbol{q}\in\mathbb{Z}^2} h_{\boldsymbol{q}} \otimes S_\parallel^n S_\perp^m \;\leftrightarrow\; H(\boldsymbol{k}) = \sum_{\boldsymbol{q}} e^{\imath \boldsymbol{k}\cdot\boldsymbol{q}}\, h_{\boldsymbol{q}}. \tag{36}$$

The $h_{\boldsymbol{q}}$'s, which coincide with $h_{x-x'}$ if $q = x - x'$, are just the Fourier coefficients of $H(\boldsymbol{k})$, which in the present context are matrices of appropriate dimension. In the following, we will often and tacitly switch between the two representations, always using the principle stated in Eq. (36).

Let G be a gap in the spectrum of H. Then the gap projection $P_G = \chi_{(-\infty,G]}(H)$, with χ the characteristic function of an interval, carries the Berry curvature [47]

$$F(\boldsymbol{k}) = (2\pi\imath)^{-1}\,\mathrm{Tr}(P_G(\boldsymbol{k})[\partial_{k_1} P_G(\boldsymbol{k}), \partial_{k_2} P_G(\boldsymbol{k})]). \tag{37}$$

Above, Tr is the trace over the two internal degrees of freedom.

The regime of CVE is defined by the following conditions. (1) Time reversal is conserved. As such, $F(\boldsymbol{k}) = -F(-\boldsymbol{k})$ and necessarily $\int_{BZ} F(\boldsymbol{k})\mathrm{d}\boldsymbol{k} = 0$. (2) The band spectrum of $H(\boldsymbol{k})$ is gutted at two points K and $K' = -K$, called the valleys. In our theory, the valleys can have structure and hence no relation to massive Dirac spectra is required. (3) There are concentrations of the Berry curvature $F(\boldsymbol{k})$ near the valleys. They may result from the splitting of a pair of Kramer degenerate Dirac nodes of the bulk bands or from Berry curvature engineering, which has nothing in common with Dirac physics. (4) In small vicinities of the valleys:

$$\int_{\mathrm{Vec}(\boldsymbol{K})} F(\boldsymbol{k})\mathrm{d}\boldsymbol{k} = -\int_{\mathrm{Vec}(\boldsymbol{K}')} F(\boldsymbol{k})\mathrm{d}\boldsymbol{k} = \frac{1}{2}. \tag{38}$$

We introduce now the DW and for this let $\mathcal{I}$ be a lattice inversion $\mathcal{I}(\xi\otimes|n,m\rangle) = W\xi\otimes|n,-m+1\rangle$, $\mathcal{I}^2 = I$, where W may act nontrivially on the internal degrees of freedom. The DW, whose center is located between the primitive cells with labels $m = 0$ and -1, divides the lattice into two disjoint sectors $\mathbb{Z}^2 = \mathcal{L}_L \cup \mathcal{L}_R$, as illustrated in Fig. 16(a). The most generic Hamiltonian for the DW configuration, excluding the disorder, takes the form

$$\widehat{H} = H_L + H_R + V_{\mathrm{DW}}, \tag{39}$$

where $H_{L/R}$ are half-space Hamiltonians with open boundary conditions:

$$H_R = \sum_{\boldsymbol{x},\boldsymbol{x}'\in\mathcal{L}_R} h_{\boldsymbol{x}-\boldsymbol{x}'}\otimes|\boldsymbol{x}\rangle\langle\boldsymbol{x}'|, \quad H_L = \mathcal{I}H_R\mathcal{I}, \tag{40}$$

and V_{DW} is a potential localized near the DW and invariant under parallel translations, gluing together the left and right sides.

The following questions need to be answered: (1) can $\widehat{H}$ posses true chiral interface bands, which emerge from one bulk band and dive in the opposite bulk band? (2) If yes, what interface potentials generate such chiral bands?

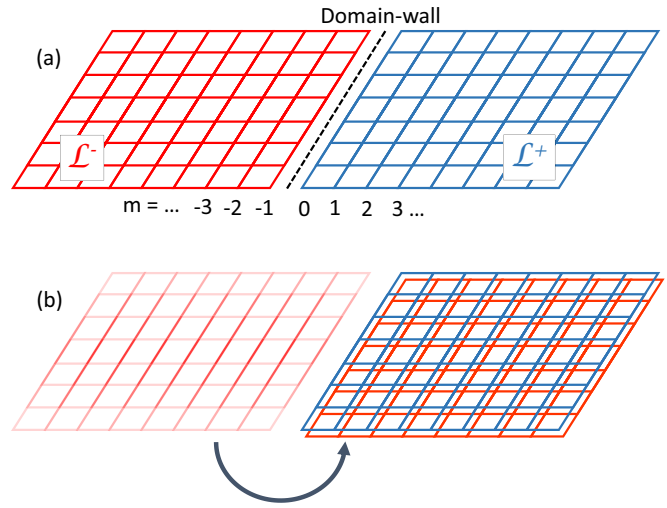

FIG. 16. Lattice folding. (a) The domain-wall configuration. (b) Folding of the lattice into an edge configuration.

B. An exact topological reference system

The formal folding of the lattice around the DW illustrated in Fig. 16(b) transforms the system into a bilayer with an edge. It only involves a proper relabeling, leading to the unitary transformation $\Gamma : \mathbb{C}^2\otimes\ell^2(\mathbb{Z}^2) \to \mathbb{C}^4\otimes\ell^2(\mathcal{L}_R)$:

$$\Gamma(\xi\otimes|n,m\rangle) = \begin{pmatrix}\xi\\0\end{pmatrix}\otimes|n,m\rangle \tag{41}$$

and

$$\Gamma(\xi\otimes|n,-m-1\rangle) = \begin{pmatrix}0\\W\xi\end{pmatrix}\otimes|n,m\rangle, \tag{42}$$

for $m \geqslant 0$. It transforms the Hamiltonian to the form

$$\widehat{\boldsymbol{H}} = \sum_{\boldsymbol{x},\boldsymbol{x}'\in\mathcal{L}_R}\begin{pmatrix}h_{\boldsymbol{x}-\boldsymbol{x}'} & 0\\ 0 & h_{\boldsymbol{x}-\boldsymbol{x}'}\end{pmatrix}\otimes|\boldsymbol{x}\rangle\langle\boldsymbol{x}'| + \boldsymbol{V}_{\mathrm{E}}, \tag{43}$$

with the potential $\boldsymbol{V}_{\mathrm{E}} = \Gamma W_{\mathrm{DW}}\Gamma^\dagger$ localized near the edge. Three important achievements to notice. (1) The DW configuration has been reduced to an edge configuration for the folded bulk Hamiltonian:

$$\boldsymbol{H} = \sum_{\boldsymbol{x},\boldsymbol{x}'\in\mathbb{Z}^2}\begin{pmatrix}h_{\boldsymbol{x}-\boldsymbol{x}'} & 0\\ 0 & h_{\boldsymbol{x}-\boldsymbol{x}'}\end{pmatrix}\otimes|\boldsymbol{x}\rangle\langle\boldsymbol{x}'|, \tag{44}$$

acting on $\mathbb{C}^4\otimes\ell^2(\mathbb{Z}^2)$. (2) Because the folded bulk system consists of two identical copies of the original system, in the vicinities of the valleys:

$$\int_{\mathrm{Vec}(\boldsymbol{K})} \boldsymbol{F}(\boldsymbol{k})\mathrm{d}\boldsymbol{k} = -\int_{\mathrm{Vec}(\boldsymbol{K}')} \boldsymbol{F}(\boldsymbol{k})\mathrm{d}\boldsymbol{k} = 1, \tag{45}$$

where this time, $\boldsymbol{F}$ is the Berry curvature of the gap projection $\boldsymbol{P}_G = \chi_{(-\infty,G]}(\boldsymbol{H})$:

$$\boldsymbol{P}_G(\boldsymbol{k}) = \begin{pmatrix}P_G(\boldsymbol{k}) & 0\\ 0 & P_G(\boldsymbol{k})\end{pmatrix}. \tag{46}$$

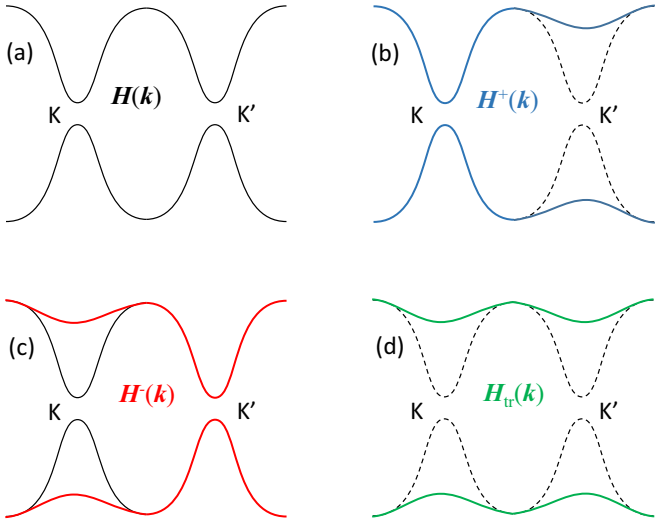

FIG. 17. Schematics of the continuous extensions. (a) The original folded Hamiltonian $\boldsymbol{H}$; (b,c) the extensions to $\boldsymbol{H}^{\pm}$, respectively. (d) The emerging trivial Hamiltonian $\boldsymbol{H}_{\rm tr}$. All Hamiltonians are represented by a section of their band spectral structure.

(3) Since the Berry curvature near a valley integrates to an integer, there is no topological obstruction against smoothly extending $\boldsymbol{P}_G(\boldsymbol{k})$ from $\mathrm{Vec}(K)$ or $\mathrm{Vec}(K')$ to the entire Brillouin torus, without adding any more Berry curvature flux.

The last two observations reflect the main differences between the simple edge and DW configurations and, as we shall see, it explains why topological modes are most of the time observed along DWs and rarely along edges. On another note, let us point out that the rigorous bulk-boundary machinery [48–50] for class A has been developed for the edge configuration, hence the folding trick enables us to extend these results to a DW configuration too. If approached directly, the bulk-boundary correspondence for a DW configuration requires additional tools [51].

We call the continuations mentioned above $\boldsymbol{P}_G^{\pm}(\boldsymbol{k})$, respectively, and note that $I - \boldsymbol{P}_G^{\pm}(\boldsymbol{k})$ provide continuous extensions of the projection corresponding to the upper spectrum. The conclusion at this point is that the folded Hamiltonian $\boldsymbol{H}(\boldsymbol{k})$ can be continuously extended over the whole Brillouin torus to topological Chern Hamiltonians $\boldsymbol{H}^{\pm}(\boldsymbol{k})$, as schematically shown in Figs. 17(b) and 17(c). Let us state explicitly that for these Hamiltonians,

$$\mathrm{Ch}(\boldsymbol{P}_G^{\pm}) = \mp 1. \tag{47}$$

Figure 18 shows how these extensions are precisely performed over the Brillouin torus. As one can see, they are performed along $k_\parallel$ such that $\boldsymbol{H}^{\pm}(\boldsymbol{k})$ and $\boldsymbol{H}$ coincide over more than half of the Brillouin torus. Furthermore, there is an overlap region $\mathcal{O}$ where $\boldsymbol{H}^{\pm}(\boldsymbol{k})$ and $\boldsymbol{H}$ all coincide. This enables us to construct the trivial Hamiltonian $\boldsymbol{H}_{\rm tr}(\boldsymbol{k})$ illustrated in Fig. 17(d), which also coincides with $\boldsymbol{H}^{\pm}(\boldsymbol{k})$ and $\boldsymbol{H}$ over the region $\mathcal{O}$. The latter has spectrum far from the gap G and its Berry curvature is null or very small.

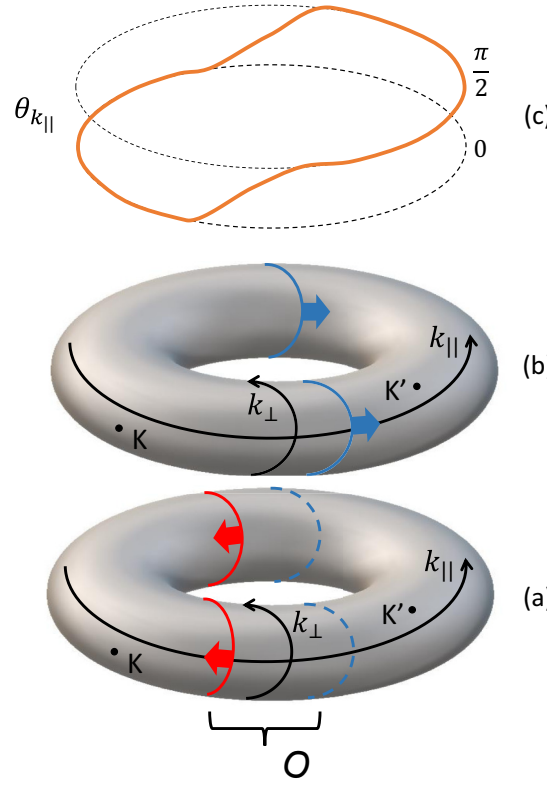

FIG. 18. The smooth extensions across the Brillouin torus. (a) $\boldsymbol{H}(\boldsymbol{k})$ is smoothly deformed from and in the direction of the blue arrows into what becomes $\boldsymbol{H}^{+}(\boldsymbol{k})$. (b) $\boldsymbol{H}(\boldsymbol{k})$ is smoothly deformed from and in the direction of the red arrows into what becomes $\boldsymbol{H}^{-}(\boldsymbol{k})$. The color coding is the same as in Fig. 17. It is important to note that the arrows are aligned with $k_\parallel$ and that there is an overlap between $\pm$ extensions, which in the text is called $\mathcal{O}$. (c) The angle $\theta_{k_\parallel}$ entering in Eq. (53).

The above procedure leads us naturally to the reference topological Hamiltonian

$$\boldsymbol{H}_{SC}(\boldsymbol{k}) = \begin{pmatrix} \boldsymbol{H}^{+}(\boldsymbol{k}) & 0 \\ 0 & \boldsymbol{H}^{-}(\boldsymbol{k}) \end{pmatrix}, \tag{48}$$

which is a spin-Chern insulator, i.e., a time-reversal symmetric system with an additional U(1) symmetry, the latter being generated by

$$\Sigma(\boldsymbol{k}) = \begin{pmatrix} I_{4\times 4} & 0 \\ 0 & -I_{4\times 4} \end{pmatrix}. \tag{49}$$

An important observation is that the reference Hamiltonian is defined over the entire Brillouin torus and, as such, it admits a real-space representation where real physical edges can be considered. As long as the U(1) symmetry is present, the two nontrivial Chern sectors of $\boldsymbol{H}_{\rm SC}$ decouple and the strong version of the bulk-boundary correspondence principle applies separately on these sectors. As such, a pair of counter-propagating boundary chiral modes emerges when the Hamiltonian (48) is halved in such a way that U(1) symmetry is preserved.

Before we move forward with the general argument, let us exemplify how these extensions can be explicitly executed

for our experimental model. Let us point out that, strictly speaking, the CVE cannot be generated with just first near neighbor couplings. However, using the data from Sec. III B, we see that the systems corresponding to $r = 1.1$, and with a little bit of stretch also $r = 1.2$, come close to our definition of VCE regime. Now, recall that $P_G(\boldsymbol{k})$ is given in (19) with $\boldsymbol{n}(\boldsymbol{k})$ specified in (21). Let us consider the simple modification given by

$$\boldsymbol{n}(\boldsymbol{k}) \;\to\; \tilde{\boldsymbol{n}}(\boldsymbol{k}) = \frac{(g\mathrm{Re}[\gamma(\boldsymbol{k})],\, g\mathrm{Im}[\gamma(\boldsymbol{k})],\, -h(k_\parallel))}{\sqrt{1+g^2|\gamma(\boldsymbol{k})|^2)}}, \quad (50)$$

where

$$h(k_\parallel) = \tanh\left(\frac{k_\parallel+\pi+p}{s}\right) - \tanh\left(\frac{k_\parallel-up}{us}\right) + \tanh\left(\frac{k_\parallel-\pi+p}{s}\right), \quad (51)$$

with u, s, and p adjustable parameters. This function takes value $+1$ on more than half of the Brillouin torus $-\pi \leqslant k_\parallel \leqslant 0$, and value -1 inside the second half, with smooth variation in between. As such, $h(\boldsymbol{k})$ changes the sign of the third component of the vector $\boldsymbol{n}$ in the region $k_1 > 0$ and, based on (20), this results in a sign change for the Berry connection of the projection $\tilde{P}_G = \frac{1}{2}(1 - \tilde{\boldsymbol{n}}\cdot\boldsymbol{\sigma})$. The continuation $\boldsymbol{P}_G^+$ of $\boldsymbol{P}_G$ is then

$$\boldsymbol{P}_G^+(\boldsymbol{k}) = \begin{pmatrix} P_G(\boldsymbol{k}) & 0 \\ 0 & \tilde{P}_G(\boldsymbol{k}) \end{pmatrix}, \quad (52)$$

whose Berry connection is simply $\boldsymbol{F}^+(\boldsymbol{k}) = F(\boldsymbol{k}) + \tilde{F}(\boldsymbol{k})$. With the change $h(k_\parallel) \to h(-k_\parallel)$, the procedure can be repeated to obtain the extension $\boldsymbol{P}_G^-(\boldsymbol{k})$. In Fig. 19, we report the Berry curvatures carried by these projections for two cases, $r = 1.1$ and $r = 1.2$. We have verified numerically that they indeed satisfy (47). Note that additional off-diagonal blocks in (52) can be trivially inserted.

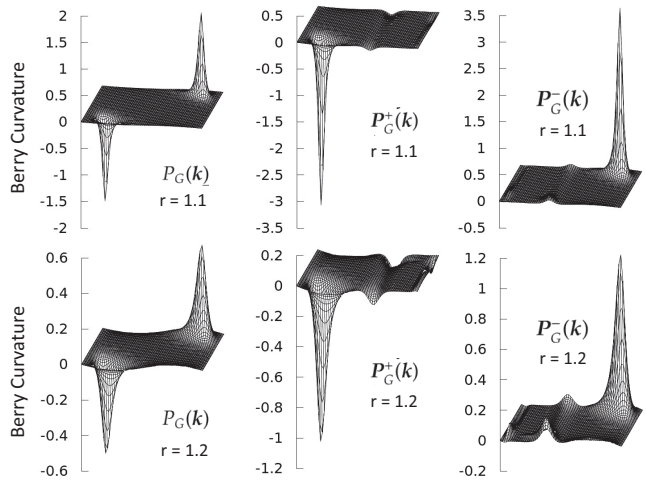

FIG. 19. Topology of the continued projections. Berry curvatures associated to the projections $P_G(\boldsymbol{k})$, $\boldsymbol{P}_G^+(\boldsymbol{k})$, and $\boldsymbol{P}_G^-(\boldsymbol{k})$, computed for $r = 1.1$ and 1.2. The parameters in (51) were fixed at $s = 0.1$, $p = 0.2$, and $u = 3$ for $r = 1.1$ and $u = 4$ for $r = 1.2$.

C. Relation with original system

In (48), the $(\pm)$ Hamiltonians act on different four-dimensional internal spaces. As such, when $\boldsymbol{H}_{\mathrm{SC}}$ is transformed back to the real space representation, it will look very different from the folded Hamiltonian $\boldsymbol{H}$ written in (44). To establish an exact connection between the two, we use the unitary transformation that rotates the eight-dimensional internal space of $\boldsymbol{H}_{\mathrm{SC}}$:

$$\boldsymbol{U}(\boldsymbol{k}) = \begin{pmatrix} \cos\theta_{k_\parallel}\cdot I_{4\times4} & -\sin\theta_{k_\parallel}\cdot I_{4\times4} \\ \sin\theta_{k_\parallel}\cdot I_{4\times4} & \cos\theta_{k_\parallel}\cdot I_{4\times4} \end{pmatrix}, \quad (53)$$

with the angle $\theta_\parallel$ specified in Fig. 18(c). Then it is straightforward to see that

$$\boldsymbol{H}_{\mathrm{VCE}}(\boldsymbol{k}) = \boldsymbol{U}(\boldsymbol{k})\,\boldsymbol{H}_{\mathrm{SC}}(\boldsymbol{k})\,\boldsymbol{U}(\boldsymbol{k})^\dagger \quad (54)$$

coincides with the original system augmented by the trivial Hamiltonian, that is,

$$\boldsymbol{H}_{\mathrm{VCE}}(\boldsymbol{k}) = \begin{pmatrix} \boldsymbol{H}(\boldsymbol{k}) & 0 \\ 0 & \boldsymbol{H}_{\mathrm{tr}}(\boldsymbol{k}) \end{pmatrix}. \quad (55)$$

Note that the remarkable identity in (54) holds in part because $\boldsymbol{H}^\pm(\boldsymbol{k})$ coincide with $\boldsymbol{H}(\boldsymbol{k})$ on the zone $\mathcal{O}$ of the Brillouin torus, where $\theta_{k_\parallel}$ has its variations. Obviously, $\boldsymbol{H}_{\mathrm{SC}}(\boldsymbol{k})$ and $\boldsymbol{H}_{\mathrm{VCE}}(\boldsymbol{k})$ are isospectral and, furthermore,

$$\mathrm{Spec}(\boldsymbol{H}_{\mathrm{SC}}) = \mathrm{Spec}(\boldsymbol{H}) \cup \mathrm{Spec}(\boldsymbol{H}_{\mathrm{tr}}). \quad (56)$$

As promised, we obtained a unitary connection between the VCE system and a genuine strong topological insulator.

We end this section by exemplifying how the extensions of the Hamiltonians can be implemented for our experimental model, specifically, for the cases $r = 1.1$ and $r = 1.2$, which are more or less close to our definition of a VCE system. The $\boldsymbol{H}^\pm(\boldsymbol{k})$ Hamiltonians can be generated by the simple procedure

$$\boldsymbol{H}^+(\boldsymbol{k}) = f'_-(\boldsymbol{k})^2\boldsymbol{P}_G^+(\boldsymbol{k}) + f'_+(\boldsymbol{k})^2(I_{4\times4} - \boldsymbol{P}_G^+(\boldsymbol{k})), \quad (57)$$

where $f'_\pm(\boldsymbol{k})$ are given by the same (18) but with $|\gamma(\boldsymbol{k})|^2$ modified to

$$\tfrac{1}{2}(1+h(k_\parallel)) * |\gamma(\boldsymbol{k})|^2 + \tfrac{1}{2}(1-h(k_\parallel)). \quad (58)$$

After changing $h(k_\parallel)$ into $h(-k_\parallel)$, we can use exactly the same procedure to obtain $\boldsymbol{H}^-(\boldsymbol{k})$. We found that best results are obtain when we double the value of u used for the continuation of the projections. A comparison between the spectrum of the original Hamiltonian $\boldsymbol{H}(\boldsymbol{k})$ and $\boldsymbol{H}^+(\boldsymbol{k})$ is provided in Fig. 20. As one can see, we indeed achieved what it was sketched in Fig. 17. Lastly, let us point out that $\theta_{k_\parallel}$ can be taken as

$$\theta_{k_\parallel} = -\frac{\pi}{4}\left(\tanh\left(\frac{k_\parallel+\pi}{s}\right) - \tanh\left(\frac{k_\parallel}{s}\right) + \tanh\left(\frac{k_\parallel-\pi}{s}\right) - 1\right). \quad (59)$$

We conclude here by pointing out that all extensions introduced in this section can be represented in real space using relation (36).

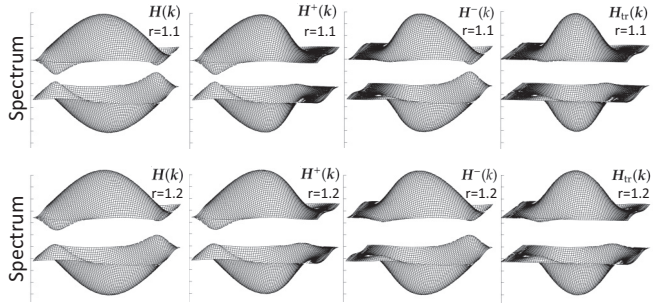

FIG. 20. Executing the continuations. The panels report the spectra of the original Hamiltonians and of the continuations (57), as well as of the trivial Hamiltonians.

D. Existence of chiral edge bands

We start with the real space representation and let $\Pi_R : \ell^2(\mathbb{Z}^2) \to \ell^2(\mathcal{L}_R)$ be the isometry:

$$\Pi_R|\boldsymbol{x}\rangle = \chi_{\mathcal{L}_R}(\boldsymbol{x})|\boldsymbol{x}\rangle, \quad \boldsymbol{x} \in \mathbb{Z}^2, \tag{60}$$

where χ is the indicator function of a set. Then, given a bulk operator $\boldsymbol{M}$, $\widehat{\boldsymbol{M}} = \Pi_R \boldsymbol{M} \Pi_R^\dagger$ is the half-space version of it with open boundary condition. Throughout, we will use the hat to indicate the halving with open boundary condition.

Since $\boldsymbol{U}$ in (53) involves only $k_\parallel$, the real space representation of $\boldsymbol{U}$ involves only $S_\parallel$, hence it commutes with Π_R. As such,

$$\widehat{\boldsymbol{H}}_{\rm VCE} = \Pi_R \boldsymbol{U}\, \boldsymbol{H}_{\rm SC}\, \boldsymbol{U}^\dagger \Pi_R^\dagger = \widehat{\boldsymbol{U}}\, \widehat{\boldsymbol{H}}_{\rm SC}\, \widehat{\boldsymbol{U}}^\dagger. \tag{61}$$

Since $\widehat{\boldsymbol{U}} = \Pi_R \boldsymbol{U} \Pi_R$ remains an unitary operator and conjugation by unitaries preserves the spectra, it follows that $\widehat{\boldsymbol{H}}_{\rm VCE}$ and $\widehat{\boldsymbol{H}}_{\rm SC}$ are isospectral. Furthermore, after a Bloch-Floquet transformation with respect to $k_\parallel$:

$$\widehat{\boldsymbol{H}}_{\rm CVE}(k_\parallel) = \widehat{\boldsymbol{U}}(k_\parallel)\, \widehat{\boldsymbol{H}}_{\rm SH}(k_\parallel)\, \widehat{\boldsymbol{U}}^\dagger(k_\parallel). \tag{62}$$

We reached one of the main conclusions of our analysis, namely, that $\widehat{\boldsymbol{H}}_{\rm CVE}$ and $\widehat{\boldsymbol{H}}_{\rm SC}$ have identical edge spectra. Since the latter displays a pair of chiral edge bands, we can conclude that $\widehat{\boldsymbol{H}}_{\rm CVE}$ does too.

The above statement was for open boundary conditions and now we show that it holds under far more general boundary conditions. For this, recall that the pair of chiral edge bands of $\widehat{\boldsymbol{H}}_{\rm SC}(k_\parallel)$ cannot be destroyed by any change of boundary condition which preserves the U(1) symmetry spelled out in Eq. (49), in particular, by the one below:

$$\widehat{\boldsymbol{H}}_{\rm SC}(k_\parallel) \to \widehat{\boldsymbol{H}}_{\rm SC}(k_\parallel) + \begin{pmatrix} \boldsymbol{V}_{\rm E}(k_\parallel) & 0 \\ 0 & \boldsymbol{V}_{\rm E}(k_\parallel) \end{pmatrix}. \tag{63}$$

Here, $\boldsymbol{V}_{\rm E}(k_\parallel)$ is any edge potential such as the physical one in Eq. (43). The particular form of $\boldsymbol{U}(\boldsymbol{k})$ [see (53)] ensures that any block-diagonal Hamiltonian commutes with $\widehat{\boldsymbol{U}}(k_\parallel)$, hence the following simple algebra holds:

$$\widehat{\boldsymbol{U}}(k_\parallel)\left[\widehat{\boldsymbol{H}}_{\rm SC}(k_\parallel) + \begin{pmatrix} \boldsymbol{V}_{\rm E}(k_\parallel) & 0 \\ 0 & \boldsymbol{V}_{\rm E}(k_\parallel) \end{pmatrix}\right] \widehat{\boldsymbol{U}}^\dagger(k_\parallel) \tag{64}$$

$$= \widehat{\boldsymbol{H}}_{\rm VCE}(k_\parallel) + \begin{pmatrix} \boldsymbol{V}_{\rm E}(k_\parallel) & 0 \\ 0 & \boldsymbol{V}_{\rm E}(k_\parallel) \end{pmatrix}.$$

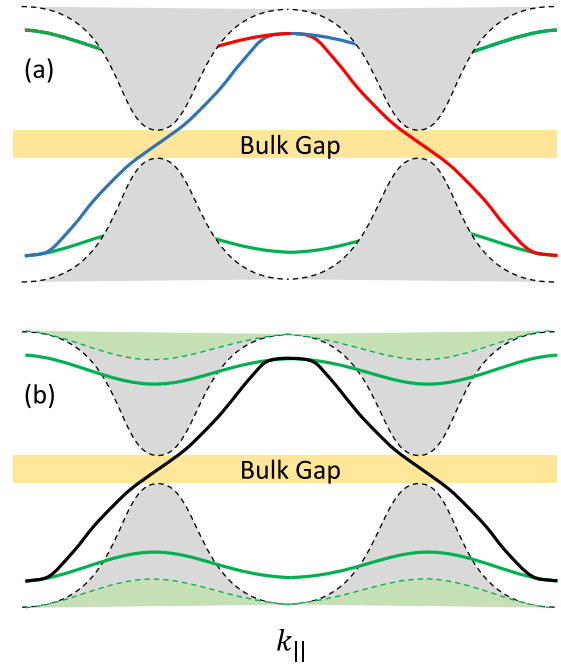

FIG. 21. Schematics of the edge spectra. (a) The topological edge spectrum of the spin-Chern Hamiltonian $\boldsymbol{H}_{\rm SC}$ consists of a pair of counter-propagating chiral bands, shown in blue and red. (b) The topological edge spectrum coincides with the reunion of the spectra of the original Hamiltonian $\boldsymbol{H}$, shown in black, and of the trivial Hamiltonian $\boldsymbol{H}_{\rm tr}$, shown in green. The shaded areas represent the bulk spectra.

This shows that the unitary equivalence between SC and CVE Hamiltonians with generic edge potentials continue to hold. Hence we can conclude that the pair of chiral edge bands of $\widehat{\boldsymbol{H}}_{\rm VCE}$ cannot be destroyed by block-diagonal edge potentials.

There is one more step in the argument. Recall that our ultimate goal is to produce a statement about the edge spectrum of the physical Hamiltonian $\widehat{\boldsymbol{H}}$ and, so far, we only have a statement about the spectrum of $\widehat{\boldsymbol{H}}_{\rm VCE}$ with any physical edge, which is just

$$\widehat{\boldsymbol{H}}_{\rm VCE} = \begin{pmatrix} \widehat{\boldsymbol{H}} + \boldsymbol{V}_{\rm E} & 0 \\ 0 & \widehat{\boldsymbol{H}}_{\rm tr} + \boldsymbol{V}_{\rm E} \end{pmatrix}.$$

Hence the pair of edge bands predicted above must coincide with the reunion of the edge spectra of $\widehat{\boldsymbol{H}}$ and $\widehat{\boldsymbol{H}_{\rm tr}}$. Recall that these two Hamiltonians coincide over the section $\mathcal{O}$ of the Brillouin torus and that $\boldsymbol{H}_{\rm tr}$ is topologically trivial. As such, under generic edge potentials, the band spectra must be as shown in Fig. 21. However, $\boldsymbol{H}_{\rm tr}$ is trivial so there are particular edge potentials $\boldsymbol{V}_{\rm E}$, which produce no edge spectrum for $\widehat{\boldsymbol{H}}_{\rm tr}$.

At this point, we reached our most important conclusion. Recall that the edge potential is connected to the DW-potential as $\boldsymbol{V}_{\rm E} = \Gamma W_{\rm DW} \Gamma^\dagger$, where Γ is the unitary transformation, which implements the folding. Then the above analysis assures us that, by adjusting the DW potential for a VCE system, as defined in Sec. IV A, one can always generate a pair of genuine chiral DW-modes.

Furthermore, using again the connection with the spin-Chern physics, we can also identify the U(1) symmetry, which

protects the modes from back-scattering. It is generated by

$$\widetilde{\Sigma}(k_\parallel) = \boldsymbol{U}\Sigma\boldsymbol{U}^{-1} = \begin{pmatrix} \cos(2\theta_{k_\parallel}) & \sin(2\theta_{k_\parallel}) \\ \sin(2\theta_{k_\parallel}) & -\cos(\theta_{k_\parallel}) \end{pmatrix}. \quad (65)$$

More precisely, any disorder potential $\boldsymbol{V}_\omega$ on the folded Hamiltonian with the property that

$$\left[\widetilde{\Sigma}\,, \begin{pmatrix} \boldsymbol{V}_\omega & 0 \\ 0 & \boldsymbol{V}_\omega \end{pmatrix}\right] = 0, \quad (66)$$

cannot Anderson-localize the domain wall modes. At this point, we have accomplished everything we promised in Introduction.

V. CONCLUSIONS

Using a versatile and highly optimized experimental platform, we uncover a fundamental difficulty in the current implementations of the QVHE. More precisely, the designs based on first nearest neighbor couplings on a honeycomb lattice will inherently fail one of the following tests: (1) Berry curvature localization around the valleys and (2) localization of the DW modes along the interface. (3) Lack of back-scattering of DW modes under lattice defects. To correct for these shortcomings, we proposed a certain Berry curvature engineering via couplings beyond nearest neighbors. We pointed out that this will force us to exit the regime where effective Dirac models can be applied and a call for new theory was put forward.

To answer this call, we introduced a new regime called valley-Chern effect, defined by large bulk spectral gaps and Berry curvature distributions localized near the valleys, both achievable, in principle, through energy bands engineering. For this regime, we demonstrated that genuine chiral DW-modes can be achieved by adjusting the DW potential. The arguments do not rely on effective models but rather on topological ones which led us to an exact unitary equivalence with a strong spin-Chern insulator.

ACKNOWLEDGMENT

All authors acknowledge support from the W.M. Keck Foundation.

[1] O. Gunawan, Y. P. Shkolnikov, K. Vakili, T. Gokmen, E. P. De Poortere, and M. Shayegan, Valley Susceptibility of an Interacting Two-Dimensional Electron System, Phys. Rev. Lett. **97**, 186404 (2006).

[2] O. Gunawan, B. Habib, E. P. De Poortere, and M. Shayegan, Quantized conductance in an AlAs 2D electron system quantum point contact, Phys. Rev. B **74**, 155436 (2006).

[3] A. Rycerz, J. Tworzydto, and C. W. J. Beenakker, Valley filter and valley valve in graphene, Nat. Phys. **3**, 172 (2007).

[4] D. Xiao, W. Yao, and Q. Niu, Valley-Contrasting Physics in Graphene: Magnetic Moment and Topological Transport, Phys. Rev. Lett. **99**, 236809 (2007).

[5] W. Yao, D. Xiao, and Q. Niu, Valley-dependent optoelectronics from inversion symmetry breaking, Phys. Rev. B **77**, 235406 (2008).

[6] S. K. FirozIslam and C. Benjamin, A scheme to realize the quantum spin-valley Hall effect in monolayer graphene, Carbon **110**, 304 (2016).

[7] Y. Ren, Z. Qiao, and Q. Niu, Topological phases in two-dimensional materials: A brief review, Rep. Prog. Phys. **79**, 066501 (2016).

[8] K. F. Mak, K. L. McGill, J. Park, and P. L. McEuen, Science **344**, 1489 (2014).

[9] R. V. Gorbachev, J. C. W. Song, G. L. Yu, A. V. Kretinin, F. Withers, Y. Cao, A. Mishchenko, I. V. Grigorieva, K. S. Novoselov, L. S. Levitov, and A. K. Geim, Science **346**, 448 (2014).

[10] M. Sui, G. Chen, L. Ma, W.-Y. Shan, D. Tian, K. Watanabe, T. Taniguchi, X. Jin, W. Yao, D. Xiao, and Y. Zhang, Nat. Phys. **11**, 1027 (2015).

[11] Y. Shimazaki, M. Yamamoto, I. V. Borzenets, K. Watanabe, T. Taniguchi, and S. Tarucha, Nat. Phys. **11**, 1032 (2015).

[12] L. Ju, Z. Shi, N. Nair, Y. Lv, C. Jin, J. Velasco, Jr., C. Ojeda-Aristizabal, H. A. Bechtel, M. C. Martin, A. Zettl, J. Analytis, and F. Wang, Topological valley transport at bilayer graphene domain walls, Nature (London) **520**, 650 (2015).

[13] I. Martin, Y. M. Blanter, and A. F. Morpurgo, Topological Confinement in Bilayer Graphene, Phys. Rev. Lett. **100**, 036804 (2008).

[14] F. Zhang, J. Jung, G. A. Fiete, Q. Niu, and A. H. MacDonald, Spontaneous Quantum Hall States in Chirally Stacked Few-Layer Graphene Systems, Phys. Rev. Lett. **106**, 156801 (2011).

[15] Z. Qiao, J. Jung, Q. Niu, and A. H. MacDonald, Electronic highways in bilayer graphene, Nano Lett. **11**, 3453 (2011).

[16] A. R. Wright and T. Hyart, Robust one-dimensional wires in lattice mismatched bilayer graphene, Appl. Phys. Lett. **98**, 251902 (2011).

[17] F. Zhang, A. H. MacDonald, and E. J. Mele, Valley Chern numbers and boundary modes in gapped bilayer graphene, Proc. Natl. Acad. Sci. USA **110**, 10546 (2013).

[18] P. San-Jose and E. Prada, Helical networks in twisted bilayer graphene under interlayer bias, Phys. Rev. B **88**, 121408(R) (2013).

[19] A. Vaezi, Y. Liang, D. H. Ngai, L. Yang, and E.-A. Kim, Topological Edge States at a Tilt Boundary in Gated Multilayer Graphene, Phys. Rev. X **3**, 021018 (2013).

[20] S. Huang, K. Kim, D. K. Efimkin, T. Lovorn, T. Taniguchi, K. Watanabe, A. H. MacDonald, E. Tutuc, and B. J. LeRoy, Topologically Protected Helical States in Minimally Twisted Bilayer Graphene, Phys. Rev. Lett. **121**, 037702 (2018).

[21] T. Ma and G. Shvets, All-Si valley-Hall photonic topological insulator, New J. Phys. **18**, 025012 (2016).

[22] X.-D. Chen and J.-W. Dong, Valley-protected backscattering suppression in silicon photonic graphene, arXiv:1602.03352.

[23] J.-W. Dong, X.-D. Chen, H. Zhu, Y. Wang, and X. Zhang, Valley photonic crystals for control of spin and topology, Nat. Mater. **16**, 298 (2017).

[24] X. Chen, M. Chen, and J. Dong, Valley-contrasting orbital angular momentum in photonic valley crystals, Phys. Rev. B **96**, 020202 (2017).

[25] O. Bleu, D. D. Solnyshkov, and G. Malpuech, Quantum valley Hall effect and perfect valley filter based on photonic analogs of transitional metal dichalcogenides, Phys. Rev. B **95**, 235431 (2017).

[26] X. Ni, D. Purtseladze, D. A. Smirnova, A. Slobozhanyuk, A. Alu, and A. B. Khanikaev, Spin- and valley-polarized one-way Klein tunneling in photonic topological insulators, Sci. Adv. **4**, eaap8802 (2018).

[27] Z. Gao, Z. Yang, F. Gao, H. Xue, Y. Yang, J. Dong, and B. Zhang, Valley surface-wave photonic crystal and its bulk/edge transport, Phys. Rev. B **96**, 201402(R) (2017).

[28] J. Noh, S. Huang, K. Chen, and M. C. Rechtsman, Observation of Photonic Topological Valley-Hall Edge States, Phys. Rev. Lett. **120**, 063902 (2018).

[29] Y. Kang, X. Ni, X. Cheng, A. B. Khanikaev, and A. Z. Genack, Pseudo-spin-valley coupled edge states in a photonic topological insulator, Nat. Commun. **9**, 2039 (2018).

[30] J. Lu, C. Qiu, M. Ke, and Z. Liu, Valley Vortex States in Sonic Crystals, Phys. Rev. Lett. **116**, 093901 (2016).

[31] J. Lu, C. Qiu, L. Ye, X. Fan, M. Ke, F. Zhang, and Z. Liu, Observation of topological valley transport of sound in sonic crystals, Nat. Phys. **13**, 369 (2017).

[32] R. K. Pal and M. Ruzzene, Edge waves in plates with resonators: An elastic analog of the quantum valley Hall effect, New J. Phys. **19**, 025001 (2017).

[33] J. Vila, R. K. Pal, and M. Ruzzene, Observation of topological valley modes in an elastic hexagonal lattice, Phys. Rev. B **96**, 134307 (2017).

[34] H. Zhu, T.-W. Liu, and F. Semperlotti, Design and experimental observation of valley-Hall edge states in diatomic-graphene-like elastic waveguides, Phys. Rev. B **97**, 174301 (2018).

[35] J.-W. Jiang, B.-S. Wang, and H. S. Park, Topologically protected interface phonons in two-dimensional nanomaterials: Hexagonal boron nitride and silicon carbide, Nanoscale **10**, 13913 (2018).

[36] F. Gao, H. Xue, Z. Yang, K. Lai, Y. Yu, X. Lin, Y. Chong, G. Shvets, and B. Zhang, Topologically protected refraction of robust kink states in valley photonic crystals, Nat. Phys. **14**, 140 (2018).

[37] T.-W. Liu and F. Semperlotti, Tunable Acoustic Valley-Hall Edge States in Reconfigurable Phononic Elastic Waveguides, Phys. Rev. Appl. **9**, 014001 (2018).

[38] Y. Wu, R. Chaunsali, H. Yasuda, K. Yu, and J. Yang, Dial-in topological metamaterials based on bistable stewart platform, Sci. Rep. **8**, 112 (2018).

[39] R. Chaunsali, C.-W. Chen, and J. Yang, Subwavelength and directional control of flexural waves in zone-folding induced topological plates, Phys. Rev. B **97**, 054307 (2018).

[40] H. Chen, H. Nassar, and G. Huang, Topological mechanics of edge waves in Kagome lattices, arXiv:1802.04404.

[41] D. Apigo, K. Qian, C. Prodan, and E. Prodan, Topological edge modes by smart patterning, arXiv:1803.00984.

[42] D. N. Sheng, Z. Y. Weng, L. Sheng, and F. D. M. Haldane, Quantum spin Hall Effect and Topologically Invariant Chern Numbers, Phys. Rev. Lett. **97**, 036808 (2006).

[43] E. Prodan, Robustness of the spin-Chern number, Phys. Rev. B **80**, 125327 (2009).

[44] See Supplemental Material at http://link.aps.org/supplemental/10.1103/PhysRevB.98.155138 for video-recordings of the DW modes along straight interfaces obtained with three different spinner configurations.

[45] See Supplemental Material at http://link.aps.org/supplemental/10.1103/PhysRevB.98.155138 for video-recordings of the DW modes along L-shaped interfaces, both clean and with defects.

[46] L. M. Nash, D. Kleckner, A. Read, V. Vitelli, A. M. Turner, and W. T. M. Irvine, Topological mechanics of gyroscopic metamaterials, Proc. Natl. Acad. Sci. USA **112**, 14495 (2015).

[47] J. E. Avron, L. Sadun, J. Segert, and B. Simon, Chern numbers, quaternions, and Berrys phases in Fermi systems, Commun. Math. Phys. **124**, 595 (1989).

[48] Y. Hatsugai, Chern Number and Edge States in the Integer Quantum Hall Effect, Phys. Rev. Lett. **71**, 3697 (1993).

[49] J. Kellendonk, T. Richter, and H. Schulz-Baldes, Edge current channels and Chern numbers in the integer quantum Hall effect, Rev. Math. Phys. **14**, 87 (2002).

[50] E. Prodan and H. Schulz-Baldes, *Bulk and Boundary Invariants for Complex Topological Insulators: From K-Theory to Physics* (Springer, Berlin, 2016).

[51] M. Kotani, H. Schulz-Baldes, and C. Villegas-Blas, Quantization of interface currents, J. Math. Phys. **55**, 121901 (2014).